Supporting Information

One-pot facile synthesis of ant-cave-structured metal oxide–carbon microballs by continuous process for use as anode materials in Li-ion batteries

You Na Ko,[1,2] *Seung Bin Park,*[2] *Kyeong Youl Jung,*[3] and *Yun Chan Kang,*[1,]*

This file includes:

- Experimental details
- Schematic diagram of the ultrasonic spray pyrolysis system.
- Crystal structures and morphologies of the precursor MoO_x and MoO_x–C composite powders directly prepared by spray pyrolysis
- Cycling performances of the precursor MoO_x and MoO_x–C composite powders directly prepared by spray pyrolysis at a constant current density of 2A g^{-1}.
- XRD patterns of the post-treated powders at 300°C under an air atmosphere.
- Thermogravimetric curve of the ant-cave-structured MoO_3–C microballs.
- TEM and dot-mapping images of ant-cave-structured MoO_3–C composite microballs at a fully charged state after 100 cycles.
- Nyquist plots of the electrochemical impedance spectra.
- Relationship between Z_{re} and $\omega^{-1/2}$ in the low-frequency region.
- SEM images of the precursor, and powders post-treated at different temperatures under a N_2 atmosphere for 3 h.
- Morphologies of the filled-structured MoO_3–C composite microballs.
- Pore size distributions of the ant-cave and filled-structured MoO_3–C composite microballs calculated by the Barrett−Joyner−Halenda (BJH) method from the adsorption isotherms.
- Pore size distributions determined by mercury porosimetry of the ant-cave and filled-structured MoO_3–C composite microballs.
- Cyclic voltammograms of the second cycles at a scan rate of 0.1 mV s^{-1}.
- Discharge/charge voltage profiles of the second cycles at a constant current density of 2 A g^{-1}.
- Electrochemical properties of MoO_x material with different morphologies.

Experimental details

Synthesis of MoO₃ and MoO₃–C powders. Ant-cave-structured molybdenum oxide–carbon composite microballs were prepared through one-pot spray pyrolysis using polystyrene (PS) beads as a template. A schematic diagram of the ultrasonic spray pyrolysis system used for the synthesis of the molybdenum oxide powders is shown in Figure S1. A 1.7-MHz ultrasonic spray generator consisting of six vibrators was used to generate a large number of droplets, which were then carried to a quartz reactor by N_2 carrier gas. The quartz reactor used had a length and diameter of 1,200 and 50 mm, respectively. The reactor temperature and flow rate of carrier gas were fixed at 900°C and 10 L min^{-1}, respectively. An aqueous spray solution was prepared by dissolving 0.1 M of MoO_3 and 0.1 M of sucrose in a mixture of hydrogen peroxide and distilled water by heating. Sucrose was used as the carbon source to form the molybdenum oxide–carbon composite powders. Finally, PS nanobeads were added to the clear solution, in a weight ratio of 2:1 with respect to MoO_3. To investigate the effects of gas atmosphere and sucrose on powder properties, the same synthesis procedures were performed under both air and N_2 atmospheres but without the addition of sucrose in the colloidal spray solutions. The as-prepared precursor powders were post-treated at 300°C for 3 h under an air atmosphere to obtain powders with the same crystal structures and to improve their electrochemical properties.

Characterizations. The morphologies of the molybdenum oxide powders prepared by spray pyrolysis were investigated through scanning electron microscopy (SEM, JEOL JSM-6060), field-emission scanning electron microscopy (FE-SEM, Hitachi S-4800), and transmission electron microscopy (FE-TEM, JEOL-2100F). The cross-sections of the ant-cave-structured MoO_3 microballs were investigated by applying a cross-section polisher (CP, JEOL SM-09010). For CP samples, the powders were mounted into an epoxy resin and carefully polished to expose the cross-section of the powders. Thermal gravimetric analysis (TGA, SDT Q600) was performed in air at a heating rate of 10°C min^{-1} to determine the amount of carbon in the powders. The crystal structures of the powders were investigated by X-ray diffractometry (XRD, X'Pert PRO MPD) using Cu Kα radiation ($\lambda = 1.5418$ Å) at the Korea Basic Science Institute (Daegu). The porosities of the powders were measured by mercury porosimeter (Auto Pore IV 9500). The surface areas of the powders were measured by the Brunauer-Emmett-Teller (BET) method using N_2 as the adsorbate gas.

Electrochemical Measurements. The electrochemical properties of the molybdenum oxide powders were analyzed in a 2032-type coin cell. The anode was prepared from a

mixture of the active material, carbon black, and sodium carboxymethyl cellulose (CMC) in a weight ratio of 7:2:1. Li metal and a microporous polypropylene film were used as the counter electrode and separator, respectively. The electrolyte was 1 M $LiPF_6$ dissolved in a mixture of fluoroethylene carbonate/dimethyl carbonate (FEC/DMC; 1:1 v/v). The discharge/charge characteristics of the samples were investigated through cycling in the voltage range 0.001–3 V at various current densities. Cyclic voltammograms were measured at a scan rate of 0.1 mV s^{-1}. Electrochemical impedance spectra was determined using AC electrochemical impedance spectroscopy (EIS) with a VersaSTAT4 over a frequency range of 0.02 Hz–100 kHz and potential amplitude of 10 mV.
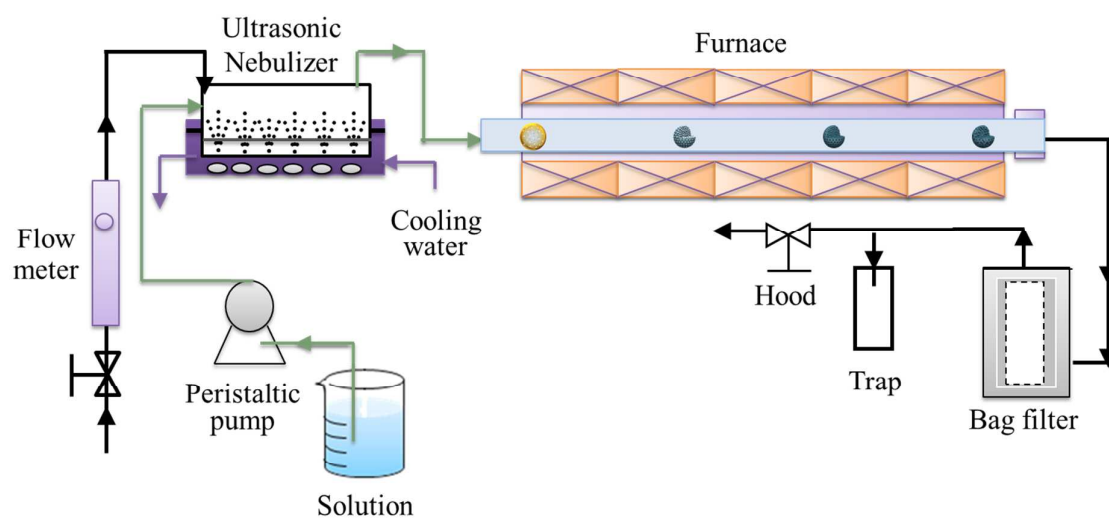
Figure S1. Schematic diagram of the ultrasonic spray pyrolysis system.
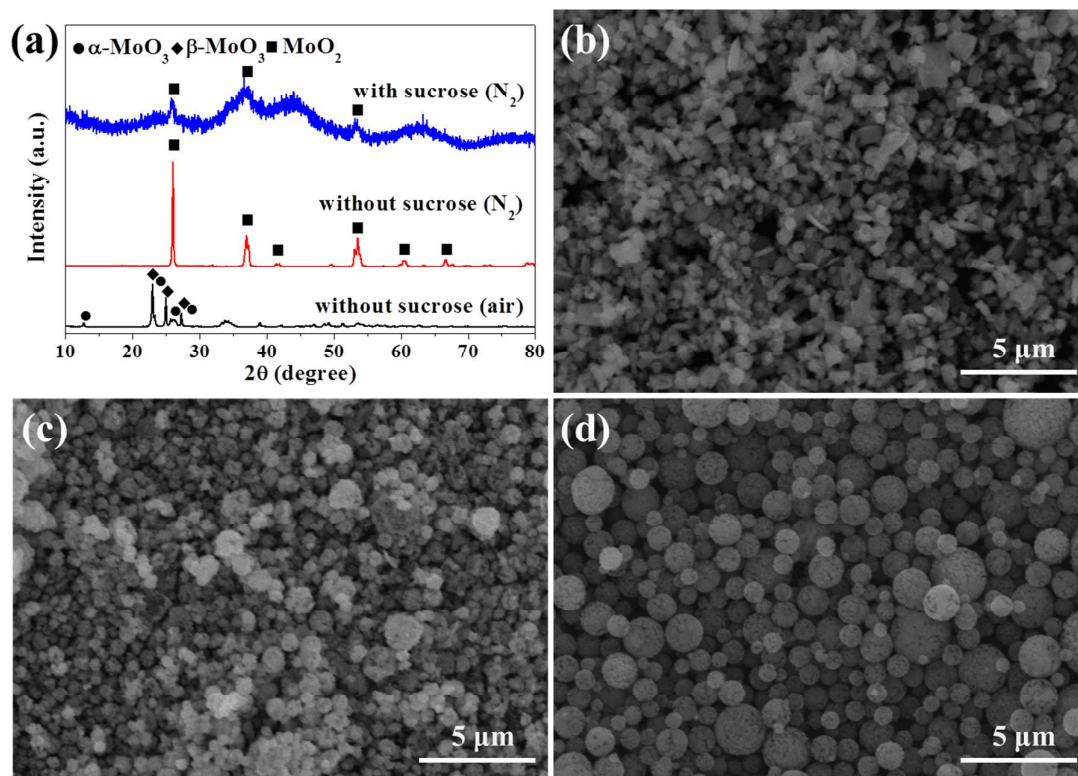
Figure S2. Crystal structures and morphologies of the precursor MoO_x and MoO_x–C composite powders directly prepared by spray pyrolysis: (a) XRD pattern, (b) SEM image of the MoO_x powders without sucrose under an air atmosphere, (c) SEM image of the MoO_x powders without sucrose under a N_2 atmosphere, and (d) SEM image of the MoO_x–C composite powders with sucrose under a N_2 atmosphere.
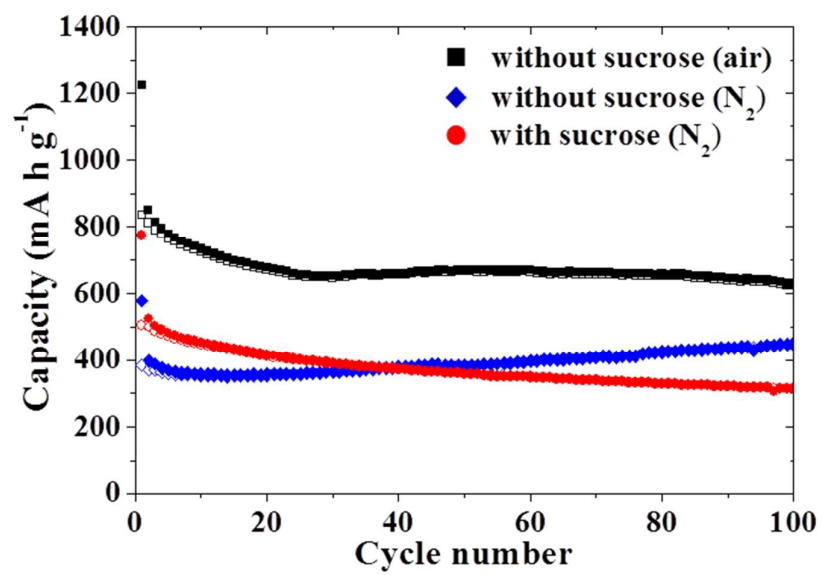
Figure S3. Cycling performances of the precursor MoO_x and MoO_x–C composite powders directly prepared by spray pyrolysis at a constant current density of 2 A g^{-1}.
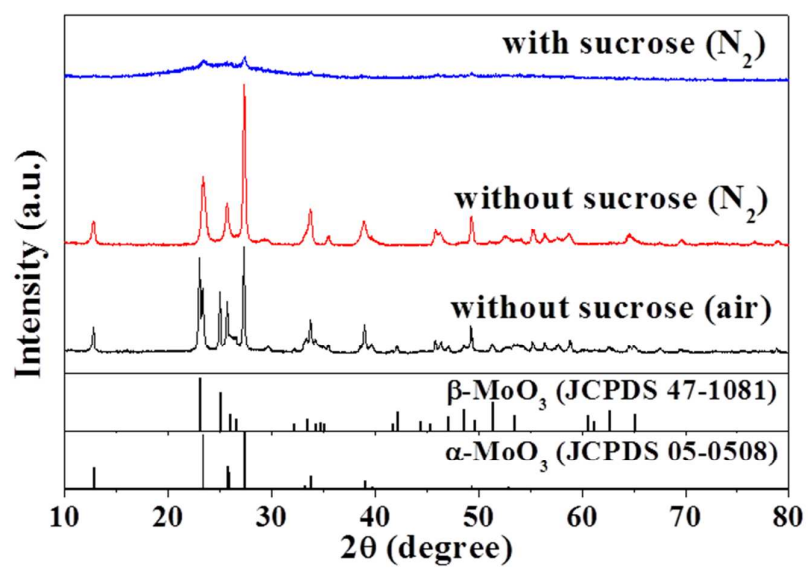
Figure S4. XRD patterns of the post-treated powders at 300°C under an air atmosphere.
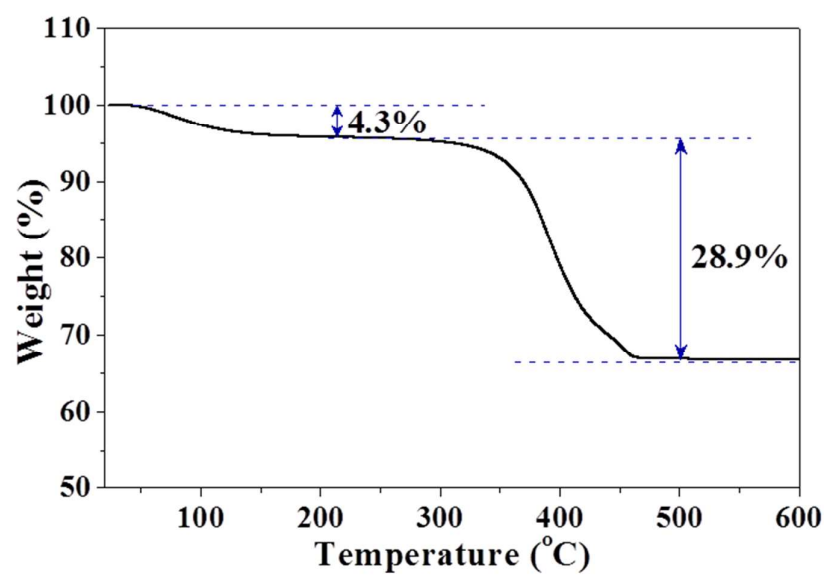
Figure S5. Thermogravimetric curve of the ant-cave-structured MoO_3–C microballs.

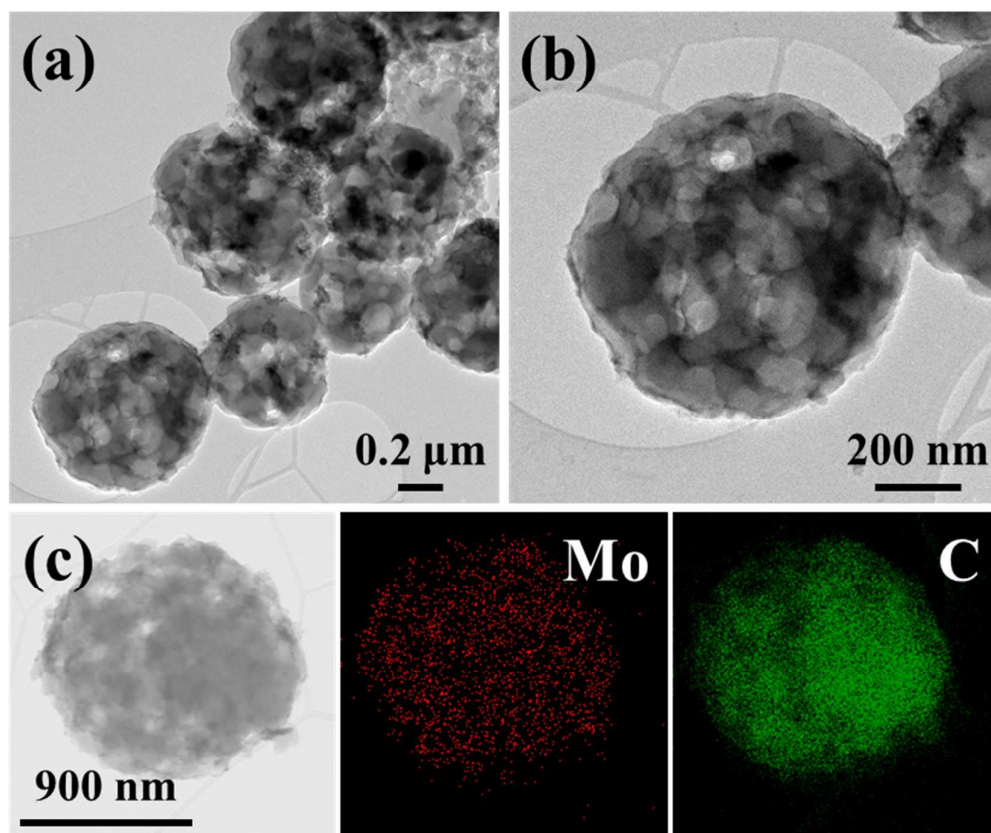**Figure S6.** TEM and dot-mapping images of ant-cave-structured MoO3–C composite microballs at a fully charged state after 100 cycles: (a) and (b) TEM images, and (c) dot-mapping images.

The electrochemical impedance spectra of the ant-cave-structured MoO_3–C composite microballs, well-faceted crystalline MoO_3 powders, and spherical MoO_3 powders were analyzed both before and after 100 cycles. The Nyquist plots (EIS spectra) as shown in Figure S7 show compressed semicircles in the medium frequency range of each spectrum, which describe the charge transfer resistance (R_{ct}) for these electrodes, and an approximately 45° inclined line in the low-frequency range, which could be considered as Warburg impedance (Z_w), which is associated with the lithium-ion diffusion in the bulk of the active material.

The radius of the ant-cave-structured MoO_3–C composite microballs was found to be smaller than that of the MoO_3 powders before cycling, which indicates that the charge–transfer resistance (R_{ct}) of the ant-cave-structured MoO_3–C composite microballs was lower. The R_{ct} of the ant-cave-structured MoO_3–C composite microballs changed slightly after 100 cycles, however, with both of the MoO_3 powders the R_{ct} significantly increased. The values of R_{ct} for the ant-cave-structured MoO_3–C composite microballs, well-faceted crystalline MoO_3 powders, and spherical MoO_3 powders after 100 cycles were calculated to be 19, 92, and 123 Ω, respectively.
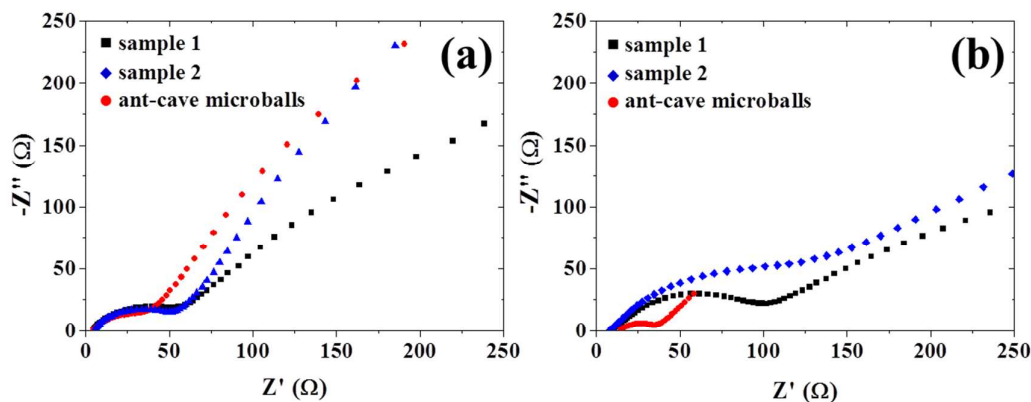

Figure S7. Nyquist plots of the electrochemical impedance spectra for ant-cave-structured MoO_3–C composite microballs, well-faceted crystalline MoO_3 powders (sample 1), and spherical MoO_3 powders (sample 2): (a) before cycling and (b) after 100 cycles at a rate of 2 A g^{-1}.

The lithium diffusion coefficient can also be calculated by using the following equation:[S1-S4]

$$D = R^2 T^2 / 2A^2 n^4 F^4 C^2 \sigma^2 \qquad (1)$$

where R is the gas constant, T is the absolute temperature, A is the surface area of the anode, n is the number of electrons transferred in the half-reaction for the redox couple, F is the Faraday constant, C is the concentration of Li ions in the solid, D is the diffusion coefficient $(cm^2\ s^{-1})$, and σ is the Warburg factor, which is relative to Z_{re}. From the slope of the lines in the inset of Figure 3b σ can be obtained.[S1-S4]

$$Z_{re} = R_D + R_L + \sigma\omega^{-1/2} \qquad (2)$$

Figure S8 shows the relationship between Z_{re} and $\omega^{-1/2}$ in the low-frequency region. According to the linear fitting, the slopes of the real part of the complex impedance versus $\omega^{-1/2}$ for the ant-cave-structured MoO_3–C composite microballs, well-faceted crystalline MoO_3 powders, and spherical MoO_3 powders after 100 cycles were 30.1, 131.7, and 422.6, respectively. The lithium diffusion coefficients at 25°C were calculated to be 2.82×10^{-10}, 1.48×10^{-11}, and $1.43 \times 10^{-12}\ cm^2\ s^{-1}$ for the ant-cave-structured MoO_3–C composite microballs, well-faceted crystalline MoO_3 powders, and spherical MoO_3 powders, respectively.

The ant-cave-structured MoO_3–C composite microballs present smaller charge transfer resistance and higher lithium diffusion coefficient than those of the MoO_3 powders. These are attributable to the fact that the ant-cave-structured MoO_3–C composite microballs are more amenable to the diffusion of Li^+ ions than MoO_3 powders.
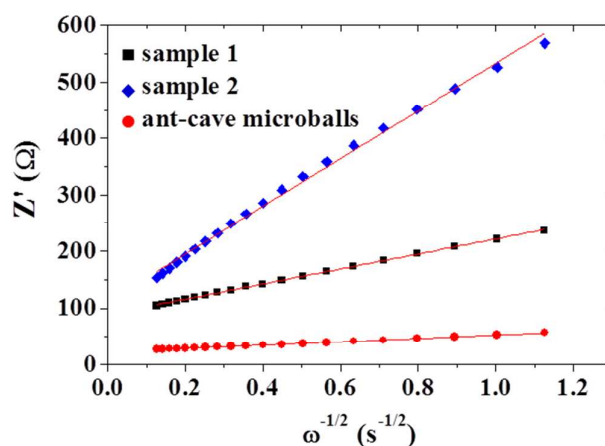

Figure S8. Relationship between Z_{re} and $\omega^{-1/2}$ in the low-frequency region.

The precursor powders were prepared by spray pyrolysis from a solution containing PS nanobeads, molybdenum salt, and sucrose at 200°C to confirm the formation process for the ant-cave-structured MoO_x–C microball. This relatively low preparation temperature prevented any decomposition of the PS nanobeads, which are known to decompose at temperatures in excess of 400°C. The morphological change of the powders with varying post-treatment temperatures was subsequently investigated. SEM images of the precursor, and powders post-treated at different temperatures under a N_2 atmosphere for 3 h, are shown in Figure S9.

Precursor powders prepared directly by spray pyrolysis exhibited a smooth surface, without the presence of any open pores. Open pores were however observed on the surface of powder particles post-treated at 500°C, as indicated by the arrows in Figure S9b. The inset on Figure S9b shows a section of fractured powder, which reveals the macroporous structure of the material. These macropores are formed by the decomposition of PS nanobeads at the post-treatment temperature of 500°C. The MoO_x–C composite powders post-treated at an even higher temperature of 800°C tended to form nanochannels, as indicated by the arrows in Figure S9c, and also exhibited large open pores throughout their surface. Partial melting and sintering of molybdenum oxide at 800°C destroyed the structure of spherical nanovoids, and the networks between these voids are responsible for creating the nanochannels inside the MoO_x–C composite powder. Consequently, an ant-cave-structured MoO_x–C microball was formed from a single droplet by one-pot spray pyrolysis, in which macroporous MoO_x-C powder is first formed as an intermediate product in the front part of a reactor maintained at 900 °C. The macroporous MoO_x–C composite powder then transformed into an ant-cave-structured MoO_x–C microball in the rear part of the reactor by partial melting and sintering of molybdenum oxide.
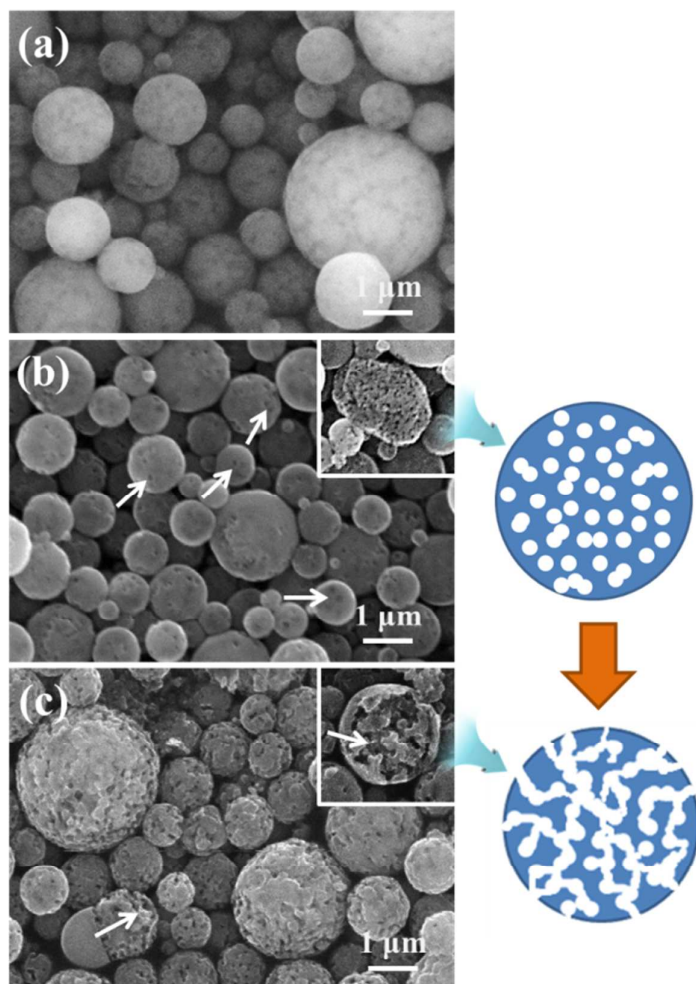
Figure S9. SEM images of the precursor, and powders post-treated at different temperatures under a N_2 atmosphere for 3 h. The precursor powders were prepared by spray pyrolysis from a solution containing PS nanobeads, molybdenum salt, and sucrose at a low preparation temperature of $200^{o}C$.

The MoO$_2$–C composite microballs were directly prepared by spray pyrolysis from an aqueous spray solution containing sucrose at 900°C under a N$_2$ atmosphere, in order to show the effect of PS nanobeads. The prepared powders were post-treated at 300°C under an air atmosphere. Figure S10 show the morphologies of the MoO$_3$–C composite microballs prepared from a spray solution without PS nanobeads. The crushed powders that are shown in Figure S10b demonstrate the resulting dense structure and absence of channels.
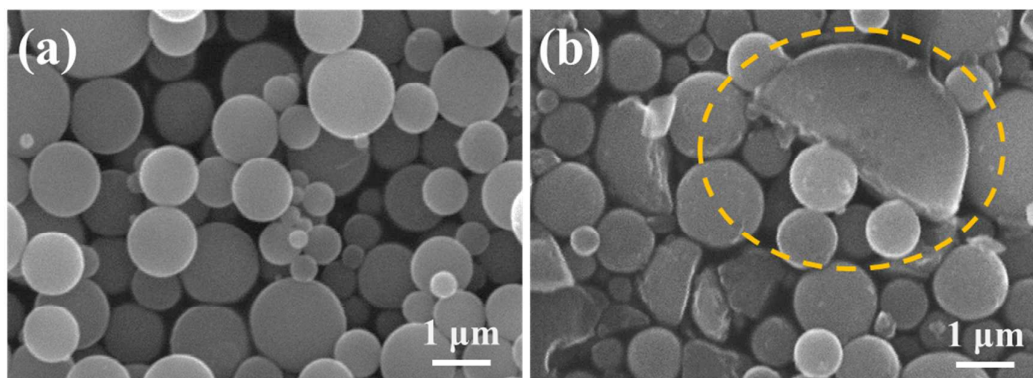

Figure S10. Morphologies of the filled-structured MoO$_3$–C composite microballs prepared directly by spray pyrolysis from the aqueous spray solution with sucrose: (a) before and (b) after crushing by hand using agate mortar.

The MoO$_3$–C composite microballs prepared from a spray solution with sucrose also contained mesopores a few nanometers in size. Figure S11 shows the pore size distribution of the MoO$_3$–C composite microballs calculated by the Barrett−Joyner−Halenda (BJH) method from the adsorption isotherms.

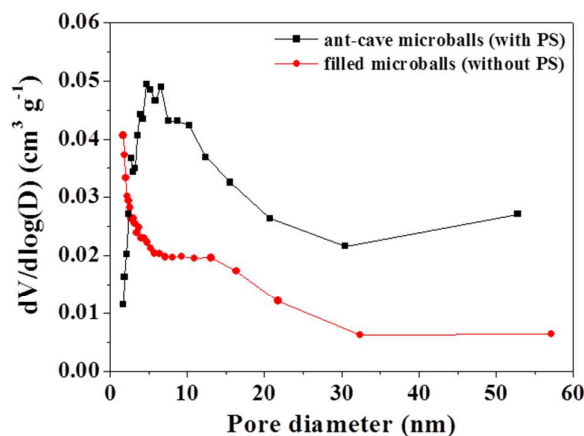**Figure S11.** Pore size distributions of the ant-cave and filled-structured MoO$_3$–C composite microballs calculated by the Barrett−Joyner−Halenda (BJH) method from the adsorption isotherms.

The pore size distribution of the ant-cave-structured MoO$_3$–C microballs was compared to that of the filled-structure MoO$_3$-C microballs. Figure S12 shows the pore size distributions for both materials, as determined by mercury porosimetry. The ant-cave-structured MoO$_3$–C microballs exhibit two distinct peaks at around 80 nm and 400 nm, with the former being related to the existence of nanochannels formed by decomposition of the polystyrene nanobeads. This 80 nm peak was not observed in the pore size distribution of the filled MoO$_3$–C microballs. The macropores detected around 400 nm in both materials can be attributed to gaps between the microballs. The ant-cave and filled-structure MoO$_3$–C microballs had porosities of 8.8 and 0.5 % within the size range of 3 to 200 nm. It is important to note that the PS nanobeads played a key role in the formation of the ant-cave-structured MoO$_3$–C microballs.

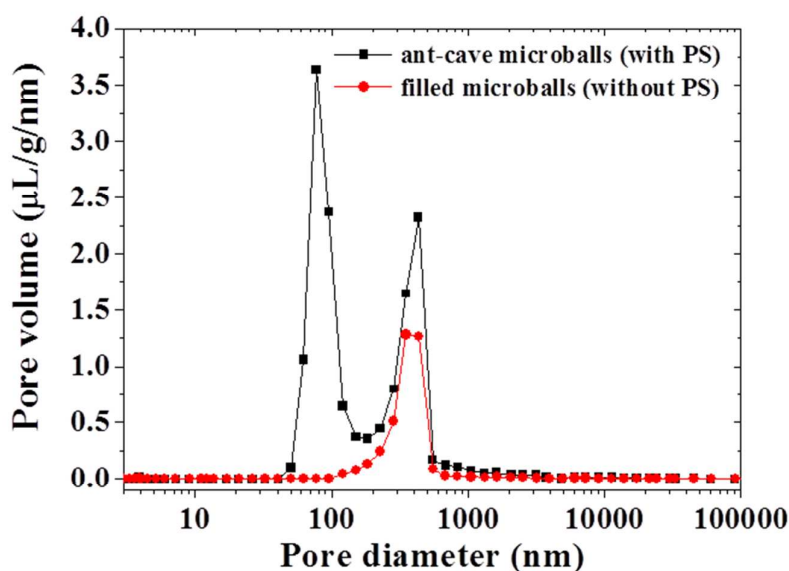**Figure S12.** Pore size distributions determined by mercury porosimetry of the ant-cave and filled-structured MoO$_3$–C composite microballs.
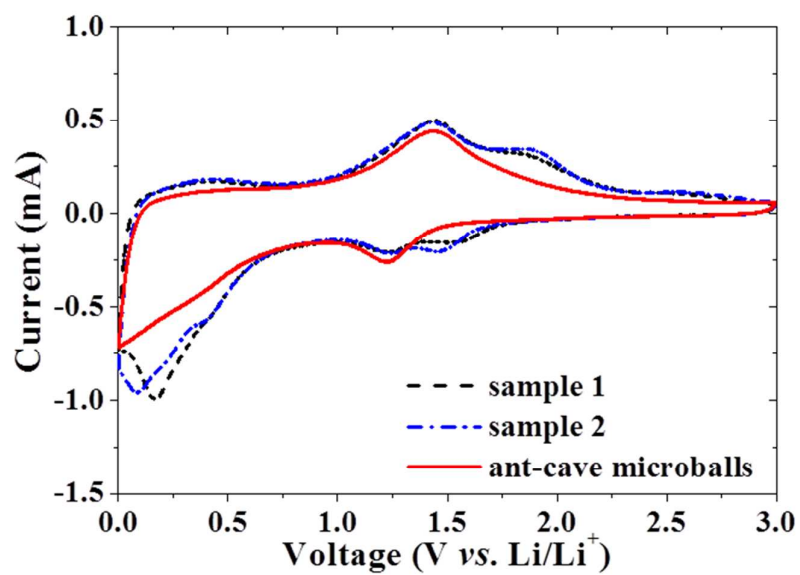
Figure S13. Cyclic voltammograms of the second cycles at a scan rate of 0.1 mV s^{-1}.
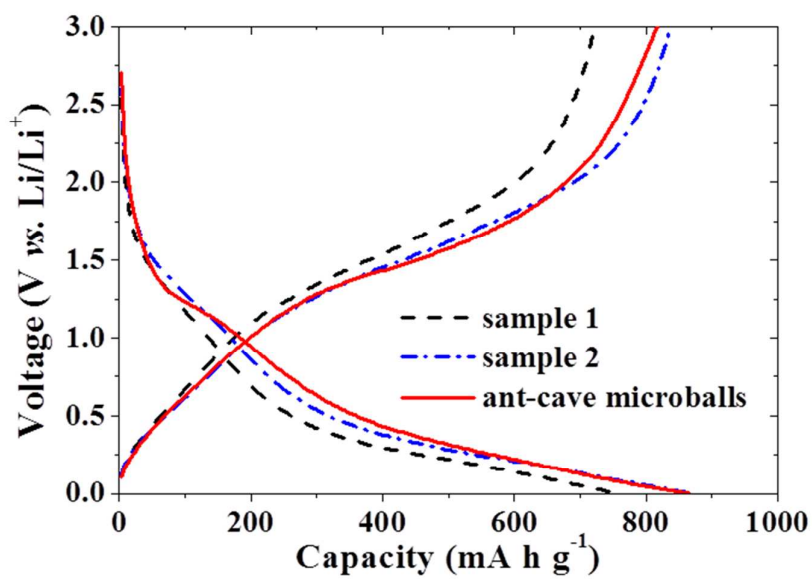
Figure S14. Discharge/charge voltage profiles of the second cycles at a constant current density of 2 A g^{-1}.

Table S1. Electrochemical properties of MoO_x material with different morphologies.

Morphology	Phase	Voltage range [V]	Current rate	Initial C_{dis}/C_{cha} [mA h g^{-1}]	Discharge capacity [mA h g^{-1}]	Cycle number	Ref
nanobelts	orthorhombic (MoO_3)	0.01-3	0.2 C	2349/1126	730	200	32
nanosphere	orthorhombic (MoO_3)	0.005-3	0.1 C	~1200/-	~1050	30	33
nanobelt	orthorhombic (MoO_3)	0.01-3	1000 mA g^{-1}	1000/-	433	80	34
yolk-shell	monoclinic (MoO_2)	0.01-3	50 mA g^{-1} 2000 mA g^{-1}	955/793 450/-	~850 427	50	38
nanowires	monoclinic (MoO_2/C)	0.01-3	1000 mA g^{-1}	-/356	327	20	39
nanoparticles embedded in carbon matrix	monoclinic (MoO_2/C)	0.01-3	50 mA g^{-1}	1207/-	734	350	40
ant-cave-structured microballs	orthorhombic (MoO_3/C)	0.001-3	2000 mA g^{-1} (about 2 C)	1212/841	733	300	this work
porous film	orthorhombic (MoO_3)	0.02-3	70 mA g^{-1}	1286/~900	803	50	S1
microrod	hexagonal (MoO_3/graphene)	0.01-3	100 mA g^{-1}	1339/987	739	30	S2
nanospheroids	orthorhombic (MoO_3)	0.005-3.5	0.5 C	~560/-	630	150	S3
hollow microsphere	orthorhombic (MoO_3)	0.01-3	1 C (1117 mA g^{-1})	1377/1148	780	100	S4
nanobelts	orthorhombic (MoO_3/C)	0.05-3	0.1 C	~1300/~1100	1064	50	S5
irregular core-shell	orthorhombic (MoO_3/C)	0.01-3	100 mA g^{-1}	1260/913	~500	100	S6
nanocomposite	orthorhombic (MoO_3/C)	0.01-3	0.2 C	945/813	700	120	S7
nanofiber	orthorhombic (MoO_3/C)	0.01-3	200 mA g^{-1}	~1000/-	~500	100	S8
nanowire array	orthorhombic ($Mo_{17}O_{47}$)	0.1-3.5	50 mA g^{-1} (first cycles 25 mA g^{-1})	~770/-	~630	20	S9
irregular shape	monoclinic (MoO_2)	0.1-3	100 mA g^{-1} (activated by cycling at 120°C)	912/842	~800	30	S10
mesorporous	rutile (MoO_2)	0.01-3	0.05 C (41.9 mA g^{-1})	960/630	750	30	S11
nanorods	monoclinic (MoO_2)	0.01-3	0.05 C	775/521	830	29	S12
hierarchical	monoclinic (MoO_2)	0.01-3	200 mA g^{-1}	587/506	719	20	S13
core-shell	monoclinic (MoO_2)	0.01-3	1 C	749/608	624	50	S14

nanobelts	monoclinic (MoO$_2$-carbon coating)	0.01-3	100 mA g^{-1}	1279/769	617	30	S15
interconnected nanocrystals	monoclinic (MoO$_2$-carbon coating)	0.01-3	200 mA g^{-1}	1040/543	~550	70	S16
nanospheres	monoclinic (MoO$_2$-carbon coating)	0.1-3	3 C	~650/-	410	60	S17
nanospheres (cage-like structure)	monoclinic (MoO$_2$/C)	0.01-3	200 mA g^{-1}	1152/811	693	80	S18
nanoparticles distributed in carbon matrix	monoclinic (MoO$_2$/C)	0.01-3	100 mA g^{-1}	1642/1044	1049	50	S19
nanocomposite with ordered mesoporous carbon	monoclinic (MoO$_2$/C)	0.02-3	50 mA g^{-1}	1278/784	689	50	S20
spherical flowerlike nanostructures	monoclinic (MoO$_2$/MWCNT)	0.01-3	100 mA g^{-1}	2270/1243	1143	200	S21
graphene composite	monoclinic (MoO$_2$/graphene)	0.01-3	1000 mA g^{-1}	468/342	~600	70	S22
graphene composite	monoclinic (MoO$_2$/graphene)	0.01-3	540 mA g^{-1}	1387/623	550	1000	S23

References

(S1) Zhao, G.; Zhang, N.; Sun, K. *J. Mater. Chem. A* **2013**, *1*, 221-224.

(S2) Tang, Q.; Wang, L.; Zhu, K.; Shan, Z.; Qin, W. *Materials Letters* **2013**, *100*, 127-129.

(S3) Lee, S. H.; Kim, Y. H.; Deshpande, R.; Parilla, P. A.; Whitney, E.; Gillaspie, D. T.; Jones, K. M.; Mahan, H.; Zhang, S.; Dillon, A. C. *Adv. Mater.* **2008**, *20*, 3627-3632.

(S4) Zhao, X.; Cao, M.; Hu, C. *Mater. Res. Bull.* **2013**, *48*, 2289-2295.

(S5) Hassan, M. F.; Guo, Z. P.; Chen, Z.; Liu, H. K. *J. Power Sources* **2010**, *195*, 2372-2376.

(S6) Xia, Q.; Zhao, H.; Du, Z.; Wang, J.; Zhang, T.; Wang, J.; Lv, P. *J. Power Sources* **2013**, *226*, 107-111.

(S7) Tao, T.; Glushenkov, A. M.; Zhang, C.; Zhang, H.; Zhou, D.; Guo, Z.; Liu, H. K.; Chen, Q.; Hu, H.; Chen, Y. *J. Mater. Chem.* **2011**, *21*, 9350-9355.

(S8) Feng, C.; Gao, H.; Zhang, C.; Guo, Z.; Liu, H. *Electrochim. Acta* **2013**, *93*, 101-106.

(S9) Meduri, P.; Clark, E.; Kim, J. H.;, Dayalan, E.; Sumanasekera, G. U. *Nano Lett.* **2012**, *12*, 1784-1788.

(S10) Ku, J. H.; Jung, Y. S.; Lee, K. T.; Kim, C. H.; Oh, S. M. *J. Electrochem. Soc.* **2009**,

156, A688-A693.

(S11) Shi, Y.; Guo, B.; Corr, S. A.; Shi, Q.; Hu, Y. S.; Heier, K. R.; Chen, L.; Seshadri, R.; Stucky, G. D. *Nano Lett.* **2009**, *9*, 4215-4220.

(S12) Guo. B.; Fang, X.; Li, B.; Shi, Y.; Quyang, C.; Hu, Y. S.; Wang, Z.; Stucky, G. D.; Chen, L. *Chem. Mater.* **2012**, *24*, 457-463.

(S13) Sun, Y.; Hu, X.; Yu, J. C.; Li, Q.; Luo, W. Yuan, L.; Zhang, W.; Huang, Y. *Energy Environ. Sci.* **2011**, *4*, 2870-2877.

(S14) Zhao, X.; Cao, M.; Liu, B.; Tian, Y.; Hu, C. *J. Mater. Chem.* **2012**, *22*, 13334-13340.

(S15) Yang, L.; Liu, L.; Zhu, Y.; Wang, X.; Wu, Y. *J. Mater. Chem.* **2012**, *22*, 13148-13152.

(S16) Zhou, L.; Wu, H. B.; Wang, Z.; Lou, X. W. *ACS Appl. Mater. Interfaces* **2011**, *3*, 4853-4857.

(S17) Wang, Z.; Chen, J. S.; Zhu, T.; Madhavi, S.; Lou, X. W. *Chem. Commun.* **2010**, *46*, 6906-6908.

(S18) Liu, B.; Zhao, X.; Tian, Y.; Zhao, D.; Hu, C.; Cao, M. *Phys. Chem. Chem. Phys.* **2013**, *15*, 8831-8837.

(S19) Chen, A.; Li, C.; Tang, R.; Yin, L.; Qi, Y. *Phys. Chem. Chem. Phys.* **2013**, *15*, 13601-13610.

(S20) Zeng, L.; Zheng, C.; Deng, C.; Ding, X.; Wei, M. *ACS Appl. Mater. Interfaces* **2013**, *5*, 2182-2187.

(S21) Bhaskar, A.; Deepa, M.; Rao, T. N. *ACS Appl. Mater. Interfaces* **2013**, *5*, 2555-2566.

(S22) Sun, Y.; Hu, X.; Luo, W.; Huang, Y. *ACS Nano* **2011**, *5*, 7100-7107.

(S23) Bhaskar, A.; Deepa, M.; Rao, T. N.; Varadaraju, U. V. *J. Power Sources* **2012**, *216*, 169-178.